nature climate change

Article

https://doi.org/10.1038/s41558-026-02598-w

Biochemical remodelling of phytoplankton cell composition under climate change

Received: 30 May 2025

Accepted: 23 February 2026

Published online: 31 March 2026

Check for updates

Shlomit Sharoni [1] ✉, Keisuke Inomura [2] ✉, Stephanie Dutkiewicz [1,3], Oliver Jahn [1], Zoe V. Finkel [4], Andrew Irwin [5], Mohammad M. Amirian [4,5], Erwan Monier [6] & Michael J. Follows [1]

Although the macromolecular composition of phytoplankton shapes the nutrition available to marine ecosystems and regulates global biogeochemistry, there are no mechanistic, predictive models for its global distribution. Here, using a cellular allocation model, we simulate phytoplankton allocation to proteins, carbohydrates and lipids in the present day and a warming scenario. Our simulations predict spatial variations consistent with available observations: in nutrient-sufficient, low-light, high-latitude regions, phytoplankton allocate more to nitrogen-rich proteins, while in nutrient-depleted subtropical regions, allocation favours carbohydrates and lipids. Under warming, subtropical phytoplankton increase protein allocation by ~20%, as subsurface populations rich in light-harvesting proteins thrive, whereas high-latitude protein allocation declines by ~15–30% due to warming and relief from light limitation. In situ macromolecular measurements in polar regions show recent trends consistent with our predictions. These results suggest that macromolecular composition responds measurably to changing environmental conditions, reshaping the nutritional landscape at the base of the marine food web.

Unicellular marine phytoplankton are responsible for half of the global conversion of carbon dioxide into organic macromolecules[1]. The production of these macromolecules, primarily proteins, lipids and carbohydrates, fuels the marine ecosystem and drives global biogeochemistry[2–6]. While phylogenetic differences exist[6–9], environmental conditions seem to play a substantial role in determining cellular macromolecular composition[10,11]. For example, low-nutrient, high-light conditions favour investment in carbon-rich carbohydrates and lipids over nitrogen-rich proteins[12–15].

Because macromolecules have distinct elemental compositions[2], shifts in their relative abundance can modify the stoichiometry of marine particulate organic matter (POM). These changes can alter ocean carbon sequestration via the biological pump[16,17], influence grazer growth rate and biomass, and affect trophic transfer efficiency[18–20].

A substantial body of literature has explored the factors controlling cellular allocation in environmental samples[7,21] (Supplementary Table 1). Previous studies characterized allometric relationships with macromolecules in phytoplankton[8] and estimated environmental macromolecular concentration using remotely sensed ocean colour data[22]. While this effort is crucial for estimating and monitoring present-day stocks, predicting responses to climate change requires a more mechanistic approach.

Here, we simulate the cellular allocation of phytoplankton to proteins, lipids and carbohydrates by implementing an allocation

[1]Department of Earth, Atmospheric and Planetary Sciences, Massachusetts Institute of Technology, Cambridge, MA, USA. [2]Graduate School of Oceanography, University of Rhode Island, Narragansett, RI, USA. [3]Center for Sustainability Science and Strategy, Massachusetts Institute of Technology, Cambridge, MA, USA. [4]Department of Oceanography, Dalhousie University, Halifax, Nova Scotia, Canada. [5]Department of Mathematics and Statistics, Dalhousie University, Halifax, Nova Scotia, Canada. [6]Department of Land, Air and Water Resources, University of California, Davis, Davis, CA, USA. ✉e-mail: sharonishlomit@gmail.com; inomura@uri.edu

https://doi.org/10.1038/s41558-026-02598-w

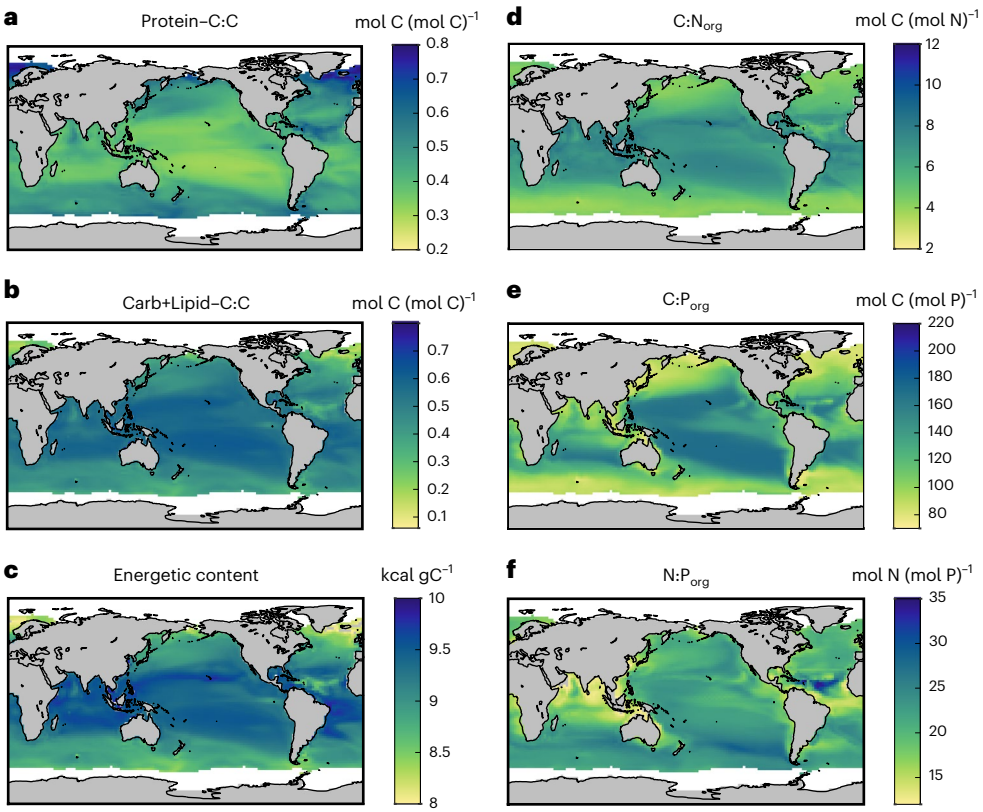

Fig. 1 | Global variations in phytoplankton composition. a,**b**, Modelled depth-integrated mean pre-industrial values of cellular allocation (mol C (mol C)$^{-1}$) to (**a**) proteins and (**b**) combined carbohydrates plus lipids. **c**, The energy content (kcal gC^{-1}) in phytoplankton cells. **d**–**f**, Elemental C:N$_{org}$ (**d**), C:P$_{org}$ (**e**) and N:P$_{org}$ (**f**) in organic matter encompassing phytoplankton, grazers and POM (molar ratios). White areas indicate regions where sea-ice cover exceeds 50%.

model that integrates experimentally derived relationships between macromolecular composition and environmental conditions[23–25], in a global ocean model. Our ecosystem is configured with two phytoplankton, broadly representing picocyanobacteria and large eukaryotes, differing in size, nutrient affinity, maximum photosynthesis rate and phosphorous storage[25] (Methods). Our simulations predict variations in macromolecular cellular allocation under present-day conditions, consistent with available observations, and reveal contrasting geographic responses to warming, simulated under a high-emissions climate change scenario (consistent with the SSP5-8.5 scenario).

Global composition of marine phytoplankton

We simulated the macromolecular composition of marine phytoplankton under pre-industrial conditions by initializing the model with observed tracer distributions and equilibrating it under a pre-industrial atmospheric CO_2 partial pressure (pCO_2) of 278 parts per million by volume (ppmv) (Methods). This simulation suggests that the average phytoplankton cell is predominantly composed of proteins (48.1%) and carbohydrates plus lipids (45%) on a molar carbon basis (mol C (mol C)$^{-1}$). Smaller contributions come from RNA, DNA, chlorophyll *a* and nitrogen storage (Extended Data Table 1). Cellular allocation exhibits global variation: allocation to proteins ranges from 32% to 78%, while carbohydrates plus lipids range from 32% to 68% of cellular carbon (Fig. 1a,b). These variations are driven by environmental conditions: in high-latitude, nutrient-sufficient, low-light environments, phytoplankton allocate more to protein, particularly those related to light harvesting (Fig. 1a). Conversely, in the mid-latitude, oligotrophic regions where nutrient concentrations are low and light is saturated, the relative growth rate of phytoplankton is low, and phytoplankton store the excess of light energy into carbon-rich storage macromolecules (Fig. 1b).

Based on the global average macromolecular composition, the average caloric content of these macromolecules[26], and assuming that carbon storage is equally divided between carbohydrates and lipids[27], we estimate a global mean energy content of 8.8 kcal gC^{-1} in marine phytoplankton (Supplementary Methods). Our model further predicts spatial variations, with caloric content varying between 8.5 kcal gC^{-1} and 10 kcal gC^{-1} (Fig. 1c), higher in the mid-latitude gyres where lipid-rich biomass dominates, and lower at the high latitudes where phytoplankton invest more in proteins (Fig. 1c).

Our pre-industrial equilibrium simulation further predicts that depth-integrated elemental ratios of total POM vary between 4 and 15 for C:N$_{org}$, 83 and 180 for C:P$_{org}$, and 11 and 33 for N:P$_{org}$ (Fig. 1d–f). These values deviate from the canonical Redfield ratio (C:N:P$_{org}$ = 106:16:1), with both lower and higher ratios, depending on the location. C:N$_{org}$ and C:P$_{org}$ are elevated at the subtropical gyres and are lower at the high latitudes. While variations in C:N$_{org}$ primarily reflect variations in cellular allocations to nitrogen-rich proteins, variations in C:P$_{org}$ are mostly a result of changes in community composition. Smaller phytoplankton, representing picocyanobacteria, with higher nutrient affinity, lower maximum biomass-specific growth rates, and reduced phosphorus storage capacity, dominate the nutrient-poor subtropical gyres. Meanwhile, larger phytoplankton, representing opportunistic eukaryotes, with higher growth rates and higher phosphorous storage capacity, dominate the nutrient-sufficient high latitudes[25,28]. N:P$_{org}$ combines these two effects, reflecting both cellular allocation strategies and shifts in community composition across environmental gradients.

To compare the model simulations with observations, we compiled a dataset of published in situ, photic zone measurements of macromolecular composition in POM (colorimetric methods) and phytoplankton (carbon isotope labelling) (Supplementary Methods and Supplementary Table 1). The simulated global means are within

https://doi.org/10.1038/s41558-026-02598-w

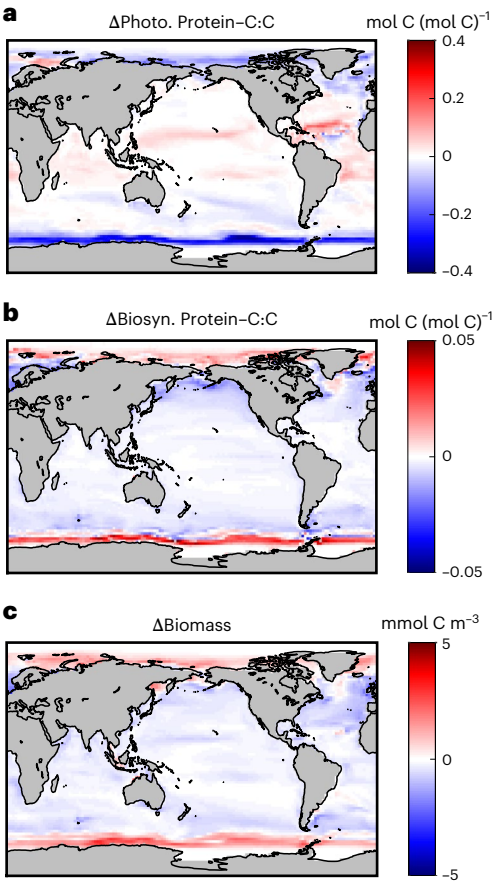

Fig. 2 | Projected change in cellular allocation to proteins and surface biomass. **a**–**c**, Drift-corrected simulated change (2070–2100 relative to 1870–1900) of depth-integrated cellular allocation (mol C (mol C)$^{-1}$) to photosynthetic (Photo.) (**a**) and biosynthetic (Biosyn.) (**b**) proteins, and surface (0–115 m) biomass (mmol C m^{-3}) (**c**).

the range of these observations (Extended Data Fig. 1). Most of the studies were conducted in polar regions, the Sea of Japan, and some restricted basins and coastal environments, which may not be well resolved in our coarse-resolution, global model. Within this dataset, we have identified three studies that measured macromolecular composition across open-ocean gradients[27,29,30], and we compare them with the model simulations. Observed sections in the North Pacific and Southern Ocean[27,30] suggest a gradual increase in protein fraction towards high latitudes, associated with a decrease in carbohydrates and lipids (Extended Data Fig. 2d,e), trends that are well captured by our model (Extended Data Fig. 2a,b). Furthermore, a long transect in the Pacific Ocean[29] indicates a negative relationship between protein content and sea surface temperature (SST), also captured in the simulations (Extended Data Fig. 2c,f). The simulations qualitatively reproduce large-scale patterns of macromolecular allocation observed in the sparse open-ocean datasets.

While data on measurements of macromolecules are scarce, larger datasets of in situ elemental composition of organic matter from 1974 to 2020 were available[31–33]. We compared the modelled C:N_{org}, C:P_{org} and N:P_{org} with the global observations by clustering the observed and modelled data into 17 ecoprovinces[34] (Extended Data Fig. 3 and Supplementary Fig. 1). Overall, the model C:N_{org}, C:P_{org} and N:P_{org} exhibit narrower distributions in the different ecoprovinces relative to the observations (Supplementary Figs. 2–4), partly because environmental conditions are less variable in the coarse-resolution simulations; however, the model consistently captures the median values and the trends along the ecoprovinces (Extended Data Fig. 3). The agreement between the model and observations in the different ecoprovinces is quantified by the distance between the modelled and observed distribution means of the log-transformed data and by the Kolmogorov–Smirnov test (Supplementary Methods), indicating that the simulations successfully capture the observed distributions (Supplementary Tables 2–4). However, there is weaker agreement between the model and observations in some regions, mainly in the North Atlantic (Extended Data Fig. 3d–f). We note that the macromolecular model does not resolve nitrogen fixation or, therefore, allocation to nitrogenase. The introduction of nitrogen fixation could partially relieve the modelled nitrate limitation and shift the North Atlantic towards phosphate limitation[35–37], which would improve the model-observed agreements specifically for C:P_{org}.

Climate-driven shifts in phytoplankton composition

Phytoplankton cellular allocation is projected to shift under a warming climate; here, we consider a high-emissions scenario (consistent with SSP5-8.5). Biochemical changes are a response to physical changes involving a mean global SST increases of 3 °C, sea-ice retreats, reduced mixing and enhanced stratification, which overall reduced the nutrient supply to the surface (Extended Data Figs. 4 and 5). Our model simulations project that, in polar regions where sea-ice retreats, photosynthetic protein levels will decline due to increased photosynthetically active radiation (PAR) (Fig. 2a). In these regions, where light limitation is relieved, phytoplankton biomass is higher, and faster-growing phytoplankton invest more in biosynthetic proteins (Fig. 2b,c). However, the increase in the biosynthetic proteins does not compensate for the concurrent reduction in light-harvesting proteins, and total protein levels are predicted to decline by 15–30% with a similar increase in carbohydrates and lipids (Fig. 3a,b).

In the temperate subpolar regions, between latitudes 40° S and 70° S, biomass is projected to decline due to higher mortality, as phytoplankton mortality rates accelerate with temperature following an Arrhenius-type relationship (Supplementary Fig. 5). In these regions, investment in biosynthetic proteins decreases because of a higher catalytic rates at the higher SST (Fig. 2b and Extended Data Fig. 4b). In these latitudes, photosynthetic proteins, which dominate the signal of the total protein, are projected to decline, specifically in the Southern Ocean, because of higher PAR driven by reduced shading (Fig. 2a,c), with overall increases in allocation to carbohydrates and lipids (Fig. 3a,b).

In the oligotrophic subtropical gyres, our model simulation projects a 20% increase in the depth-integrated cellular photosynthetic protein (Fig. 2a). This increase results from contrasting responses of the surface and subsurface phytoplankton. At the surface (0–75 m), phytoplankton biomass is projected to decline by ~50%, due to enhanced stratification and reduced nitrogen delivery into the surface (Extended Data Fig. 6c). By contrast, in the subsurface layer (75–170 m), phytoplankton biomass is projected to increase by ~40% (Extended Data Fig. 6d) due to enhanced stratification, reduced nutrient availability and higher SST. Subsurface phytoplankton have more photosynthetic proteins to capture light more efficiently. Thus, the downward shift of phytoplankton biomass in the water column brings higher allocation to photosynthetic proteins and, overall, increases the depth-integrated cellular protein allocation (Extended Data Fig. 6e). Because the change in photosynthetic proteins is the largest, it controls the total cellular protein change (Fig. 3a and Extended Data Fig. 6e). We note that the introduction of nitrogen fixers into our model would partially mute these projected changes in biomass and protein levels, specifically in the subtropics where iron is relatively abundant[38,39]. Nevertheless, the mechanisms and signs of the projected responses are robust. Furthermore, such vertical profiles of a higher subsurface productivity were observed in the highly oligotrophic subtropical gyres (in the ALOHA station), indicating that such a scenario is feasible[39].

https://doi.org/10.1038/s41558-026-02598-w

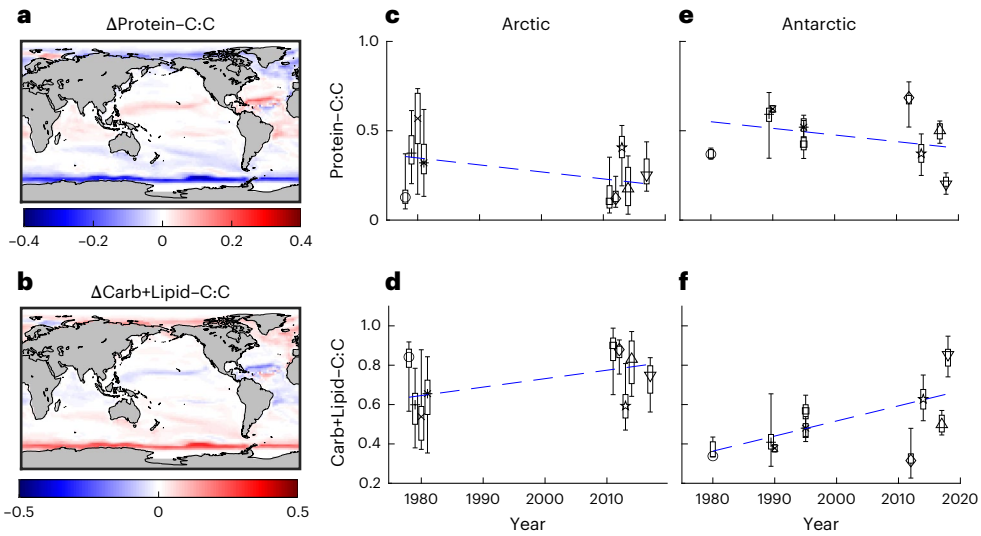

Fig. 3 | Temporal trends in macromolecular composition in polar phytoplankton. a,**b**, Modelled drift-corrected simulated change (2070–2100 relative to 1870–1900) of depth-integrated cellular allocation (mol C (mol C)$^{-1}$) to total proteins (**a**) and combined carbohydrates and lipids (**b**). **c**,**d**, Observed Arctic protein (n_{obs} = 307) (**c**) and combined Arctic carbohydrate plus lipid content (n_{obs} = 302) (**d**). Arctic data were obtained from: Irwin et al., 1980[45] (circle), Irwin et al., 1984[46] (plus), Irwin et al., 1983a[47] (cross), Irwin et al., 1983b[48] (star), Kim et al., 2015[51] (square), Yun et al., 2015[11] (diamond), Ahn et al., 2019[72] (pentagon), Choe et al., 2021[52] (upward triangle) and Kim et al., 2020[46] (downward triangle). **e**,**f**, Observed Antarctic protein (n_{obs} = 85) (**e**) and combined Antarctic carbohydrate and lipid (n_{obs} = 93) (**f**). Antarctic data were obtained from: Handa and Tanoue 1983[30] (circle), Fabiano et al., 1993[54] (plus), Fabiano et al., 1996[55] (cross), Fabiano and Pusceddu 1998[56] (star), Pusceddu et al., 1999[57] (square), Kim et al., 2016[58] (diamond), Kim et al., 2018[10] (pentagon), Misic et al., 2024[59] (upward triangle) and Jo et al., 2021[60] (downward triangle). Box plots in **c**–**f** show the median (50th percentile) as the centre line, with the interquartile range (25th–75th percentiles) represented by the box boundaries. Whiskers represent the 5th and 95th percentiles of the data. Only data obtained with colorimetric methods are included. For linear regression statistics, see Supplementary Table 5.

In response to these changes, phytoplankton energy and elemental content are projected to change (Fig. 4). At high latitudes, the depth-integrated caloric content is projected to increase by ~3.5% (that is, 0.3 kcal gC^{-1}) due to a reduction in protein and increase in lipids, which are calorie dense. At polar latitudes where ice retreats, the depth-integrated caloric content is projected to increase even further, that is, by 12% (that is, 1 kcal gC^{-1}) due to an increase in the lipid content of the organic matter at the expense of photosynthetic proteins. In the oligotrophic subtropical gyres, the depth-integrated caloric content is projected to decrease by ~3.5% (0.3 kcal gC^{-1}) due to an increase in proteins and a reduction in cellular allocation to lipids (Fig. 4a).

Depth-integrated C:N_{org} values are projected to increase by ~3–18% at high latitudes owing to lower protein levels driven by a reduced supply of bioavailable nitrogen, and decrease by 6–7% in the oligotrophic subtropical gyres where protein level increases owing to enhancement in subsurface phytoplankton, consistent with previous studies[38,40] (Fig. 4b). In the poles, a reduction of ~30% proteins leads to only about a 1-unit change in C:N_{org}, partly because light- or iron-limited growing phytoplankton cells increase their nitrogen storage (Extended Data Fig. 7). Consequently, change in elemental composition are less likely to stand out from background environmental variability. This indicates that the macromolecular composition of freshly produced organic matter may be a more sensitive indicator of changing environmental conditions than elemental ratios.

C:P_{org} is projected to increase at high latitudes by 6–18% as small phytoplankton become more dominant as a result of a reduction in nutrient supply rates (Fig. 4c and Extended Data Fig. 5c,f). Variation in N:P_{org} is a result of two competing mechanisms: higher abundance of small phytoplankton is predicted to increase N:P_{org} (Fig. 4d, red regions), and a reduction in cellular proteins is predicted to decrease N:P_{org}.

The higher projected C:P_{org} and C:N_{org} projected by our model would increase the capacity of the ocean to store more carbon by the biological pump relative to a fixed stoichiometry case[17], and may mute a projected decrease in organic carbon export of 9–16% in response to the decline in net primary productivity[41] (Extended Data Figs. 4 and 5). These findings are consistent with previous studies[38,40] that used internal-stores models of phytoplankton; the macromolecular framework also provides a dynamic, biologically mechanistic underpinning. The increase in C:N_{org} is due to a reduction in protein at the expense of carbon-rich lipids and carbohydrates, whereas the increase in cellular C:P_{org} results from a community shift towards smaller phytoplankton with lower phosphorus storage.

Observed polar shift in phytoplankton macromolecules

In the subtropical gyres, macromolecular measurements with sufficient temporal resolution are limited (Supplementary Table 1). By contrast, the polar regions provide a unique opportunity to test our model predictions, as they have been sampled since the 1970s owing to their critical role in global primary productivity and fisheries[42–44]. Measurements of macromolecules in the Arctic between 1978 and 2004 suggest a relatively high protein content in bulk POM (median 0.35), with carbohydrates and lipids together accounting for 0.60 (refs. 45–48) (Fig. 3c,d and Supplementary Table 1). Incubations of Arctic phytoplankton with inorganic labelled carbon from 1980 to 2004 also indicate a high fraction of photosynthetic carbon allocated to protein[44,49,50] (Extended Data Fig. 8 and Supplementary Table 1). Later measurements between the years 2011 and 2017 suggest lower protein content and higher lipid plus carbohydrate in POM[11,51–53] (median 0.14 and 0.86, respectively; Fig. 3c,d). Overall, the observed decline in protein and the corresponding increase in carbohydrates plus lipids in the Arctic over recent decades are small but statistically significant (Supplementary Table 5). In the Antarctic, most studies[10,30,54–60] show a declining trend in protein and an increase in the sum of lipid and carbohydrates in bulk POM (Fig. 3e,f, Extended Data Fig. 8c,d and Supplementary Tables 5 and 6). An exception is Smith and Morris (1980)[43], who estimated significantly higher carbon incorporation into lipids in

https://doi.org/10.1038/s41558-026-02598-w

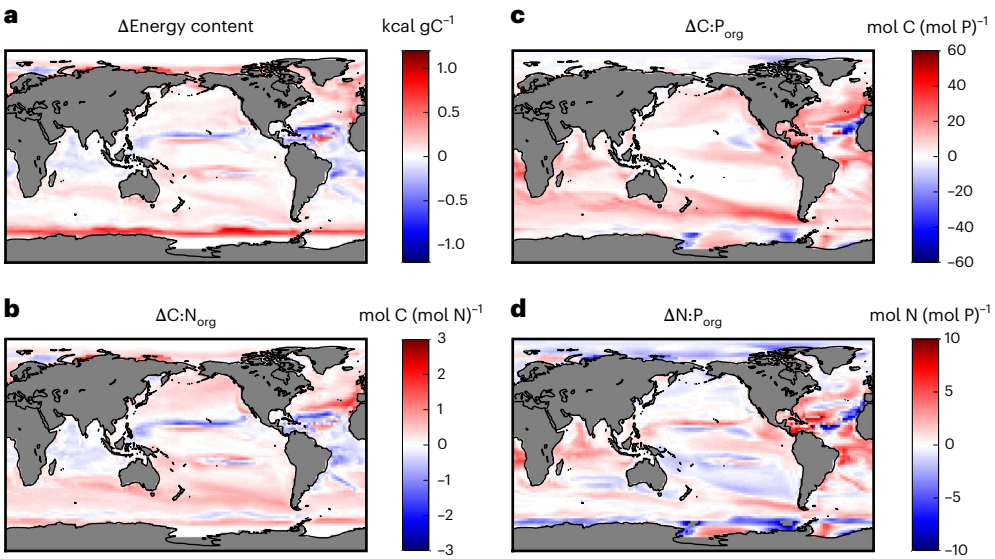

Fig. 4 | Projected change in energy content and elemental composition. a–d, Drift-corrected simulated change (2070–2100 relative to 1870–1900) of depth-integrated energy content of phytoplankton cell (kcal gC^{-1}) (**a**), $C:N_{org}$ (**b**), $C:P_{org}$ (**c**) and $N:P_{org}$ (**d**) in organic matter encompassing phytoplankton, grazers and POM (molar ratios).

phytoplankton using isotope labelling techniques. These trends in the polar regions, which emerge from different studies across different sampling environments and analytical procedures (Supplementary Table 1), are in qualitative agreement with our model-projected decline in protein content and the increase in carbohydrates plus lipids. Notably, this trend is evident in the Arctic, where warming over the past two decades has been more than double the global average, and the region has experienced the most rapid sea-ice loss[61]. Thus, the Arctic is the most likely region for such a signal to appear first.

Ecological consequences for the marine ecosystem

Our model simulations project that at high latitudes phytoplankton will invest ~10% less in cellular proteins, with a similar increase in investment in carbohydrates and lipids by the end of the twenty-first century (Fig. 3a,b). In polar regions, these changes are exacerbated, with cells investing ~15–30% less in cellular proteins with a similar increase in lipids and carbohydrates. We detected these trends in Arctic samples collected between 1978 and 2018, suggesting a decline in protein allocation and an increase in allocation to carbohydrates plus lipid (Fig. 3). Our mechanistic model suggests that increasing light availability due to ice melting reduces investment in photosynthetic proteins, although macromolecular remodelling in the field is probably influenced by multiple environmental factors. Our model further suggests that these rearrangements will increase the caloric content of organic matter as lipids are more calorie dense (Fig. 4a). While the caloric content of planktonic biomass may be higher in high latitudes, the nutritional value will probably decline (that is, higher global $C:N_{org}$ and $C:P_{org}$, lower proteins and higher calories; Fig. 4a–c).

Such degradation in the nutritional value of marine primary productivity echoes the 'dilution effect' of CO_2 fertilization in terrestrial plants, which drives a decline in their nutritional content[62,63]. However, in marine phytoplankton, the mechanism of change of the food quality is different and is driven by a combination of warming, stratification, ice melting and nutrient reduction, which globally increases carbon-rich, nitrogen-poor macromolecules such as lipids and carbohydrates at the expense of proteins (Fig. 3a,b).

The biochemical alteration of food quality can further impact higher tropic levels. Experimental studies have shown that the egg production and growth rate of marine copepods feeding on nitrogen-depleted algae were dramatically reduced due to lack of essential proteins and prey selectivity[18,64–66]. This effect of food quality in algae was channelled up the food web, ultimately reducing larval fish survival[5,67]. Therefore, a projected decline in proteins and bioavailable nitrogen at high latitudes can negatively influence zooplankton and fish populations.

In polar regions, the marine food web heavily relies on polyunsaturated fatty acids. It has been documented that polar grazers have evolved specific strategies to accumulate lipids from low-energy phytoplankton to survive prolonged periods of continuous darkness[68]. Higher projected lipid and energy content of polar phytoplankton by the end of the twenty-first century may benefit zooplankton lipid accumulation, enhance their winter survival and support the entire polar ecosystem[69]. However, the timing of phytoplankton–zooplankton interaction in the Arctic is synchronized. Melting of sea ice and rising temperatures have already altered the timing and duration of phytoplankton blooms, creating a mismatch in predator–prey interactions[70]. Our findings that phytoplankton alter their biochemical composition might cause an additional biochemical mismatch between the predator and prey, which would further alter grazer's reproductive cycles, with consequences for the entire Arctic marine ecosystem.

Phytoplankton in the subtropical oligotrophic gyres support a diverse pelagic ecosystem. Under warming, this ecosystem will suffer from lower surface nutrient input due to enhanced stratification. The increase in protein-rich, subsurface phytoplankton biomass projected by our model may counteract the reduction in surface primary productivity. This protein enrichment of phytoplankton biomass could potentially enhance their quality as a food source, positively affecting local biodiversity, the vertical migration of zooplankton and pelagic fish, and the sustainability of deep pelagic communities[71].

Conclusions

We identify how the macromolecular composition of phytoplankton is shaped by environmental conditions. Currently, in nutrient-rich, low-light, high-latitude regions, phytoplankton are protein-dense, whereas in nutrient-poor, oligotrophic subtropical gyres, they are enriched in carbohydrates and lipids. Our model projects geographically variable responses to warming: by the end of the twenty-first century, under a high-emissions scenario, phytoplankton at high latitudes will have more carbohydrates and lipids at the expense of proteins. We

detected early signs of these temporal trends in our compiled dataset, specifically in Arctic phytoplankton, where the environment is undergoing extremely rapid change. Such alteration in the macromolecular composition of marine phytoplankton will alter the nutrients and calories available for higher trophic layers, eventually affecting the natural resource availability for human beings. Our findings emphasize the importance of continuously monitoring changes in the macromolecular composition of phytoplankton, not only because of their significance to the marine ecosystem and global biogeochemistry, but also because their biochemical composition serves as an indicator of changing environmental conditions.

Online content

Any methods, additional references, Nature Portfolio reporting summaries, source data, extended data, supplementary information, acknowledgements, peer review information; details of author contributions and competing interests; and statements of data and code availability are available at https://doi.org/10.1038/s41558-026-02598-w.

References

1. Field, C. B., Behrenfeld, M. J., Randerson, J. T. & Falkowski, P. Primary production of the biosphere: Integrating terrestrial and oceanic components. *Science* **281**, 237–240 (1998).
2. Sterner, R. W. & Elser, J. J. *Ecological Stoichiometry: the Biology of Elements from Molecules to the Biosphere* (Princeton Univ. Press, 2002).
3. Ware, D. M. & Thomson, R. E. Bottom-up ecosystem trophic dynamics determine fish production in the Northeast Pacific. *Science* **308**, 1280–1284 (2005).
4. Moe, S. J. et al. Recent advances in ecological stoichiometry: Insights for population and community ecology. *Oikos* **109**, 29–39 (2005).
5. Malzahn, A. M., Aberle, N., Clemmesen, C. & Boersma, M. Nutrient limitation of primary producers affects planktivorous fish condition. *Limnol. Oceanogr.* **52**, 2062–2071 (2007).
6. Finkel, Z. V. et al. Phylogenetic diversity in the macromolecular composition of microalgae. *PLoS ONE* **11**, e0155977 (2016).
7. Morris, I. Photosynthetic products, physiological state, and phytoplankton growth. *Can. Bull. Fish. Aquat. Sci.* **210**, 83–102 (1981).
8. Finkel, Z. V., Follows, M. J. & Irwin, A. J. Size-scaling of macromolecules and chemical energy content in the eukaryotic microalgae. *J. Plankton Res.* **38**, 1151–1162 (2016).
9. Amirian, M. M., Irwin, A. J. & Finkel, Z. V. Extending the Monod model of microbal growth with memory. *Front. Mar. Sci.* **9**, 963734 (2022).
10. Kim, B. K. et al. Vertical distributions of macromolecular composition of particulate organic matter in the water column of the Amundsen Sea Polynya during the summer in 2014. *J. Geophys. Res. Oceans* **123**, 1393–1405 (2018).
11. Yun, M. S. et al. Comparison of phytoplankton macromolecular compositions and zooplankton proximate compositions in the northern Chukchi Sea. *Deep Sea Res. Pt. II* **120**, 82–90 (2015).
12. Piorreck, M. & Pohl, P. Formation of biomass, total protein, chlorophylls, lipids, and fatty acids in green and blue-green algae during one growth phase. *Phytochemistry* **23**, 217–223 (1984).
13. Breuer, G., Lamers, P. P., Martens, D. E., Draaisma, R. B. & Wijffels, R. H. The impact of nitrogen starvation on the dynamics of triacylglycerol accumulation in nine microalgae strains. *Bioresour. Technol.* **124**, 217–226 (2012).
14. Frada, M. J., Burrows, E. H., Wyman, K. D. & Falkowski, P. G. Quantum requirements for growth and fatty acid biosynthesis in the marine diatom *Phaeodactylum tricornutum* (Bacillariophyceae) in nitrogen replete and limited conditions. *J. Phycol.* **49**, 381–388 (2013).
15. Liefer, J. D. et al. The macromolecular basis of phytoplankton C:N:P under nitrogen starvation. *Front. Microbiol.* **10**, 763 (2019).
16. Volk, T. & Hoffert, M. I. in *The Carbon Cycle and Atmospheric CO_2: Natural Variations Archean to Present* (eds Sundquist, E. T. & Broecker, W. S.) 99–110 (AGU, 1985).
17. Galbraith, E. D. & Martiny, A. C. A simple nutrient-dependence mechanism for predicting the stoichiometry of marine ecosystems. *Proc. Natl Acad. Sci. USA* **112**, 8199–8204 (2015).
18. Mitra, A. & Flynn, K. J. Predator-prey interactions: Is 'ecological stoichiometry' sufficient when good food goes bad?. *J. Plankton Res.* **27**, 393–399 (2005).
19. Koch, U., Von Elert, E. & Straile, D. Food quality triggers the reproductive mode in the cyclical parthenogen Daphnia (Cladocera). *Oecologia* **159**, 317–324 (2009).
20. Thomas, P. K., Kunze, C., Van de Waal, D. B., Hillebrand, H. & Striebel, M. Elemental and biochemical nutrient limitation of zooplankton: a meta-analysis. *Ecol. Lett.* **25**, 2776–2792 (2022).
21. Bhavya, P. S. et al. A review on the macromolecular compositions of phytoplankton and the implications for aquatic biogeochemistry. *Ocean Sci. J.* **54**, 1–14 (2019).
22. Roy, S. Distributions of phytoplankton carbohydrate, protein and lipid in the world oceans from satellite ocean colour. *ISME J.* **12**, 1457–1472 (2018).
23. Inomura, K. et al. A mechanistic model of macromolecular allocation, elemental stoichiometry, and growth rate in phytoplankton. *Front. Microbiol.* **11**, 86 (2020).
24. Armin, G. & Inomura, K. Modeled temperature dependencies of macromolecular allocation and elemental stoichiometry in phytoplankton. *Comput. Struct. Biotechnol. J.* **19**, 5421–5427 (2021).
25. Inomura, K., Deutsch, C., Jahn, O., Dutkiewicz, S. & Follows, M. J. Global patterns in marine organic matter stoichiometry driven by phytoplankton ecophysiology. *Nat. Geosci.* **15**, 1034–1040 (2022).
26. Daugherty, N. A. & Watkins, K. W. Energy value of foods. *J. Chem. Educ.* https://doi.org/10.1021/ed053p80 (1973).
27. Liefer, J. D. et al. Latitudinal patterns in ocean C:N:P reflect phytoplankton acclimation and macromolecular composition. *Proc. Natl Acad. Sci. USA* **121**, e2404460121 (2024).
28. Sharoni, S. & Halevy, I. Nutrient ratios in marine particulate organic matter. *Sci. Adv.* **6**, eaaw9371 (2020).
29. Handa, N., Yanagi, K. & Matsunaga. Distribution of detrital materials in the Western Pacific Ocean and their biochemical nature. *Mem. Natl Inst. Polar Res.* 53–71 (1973).
30. Handa, N. & Tanoue, E. Organic compounds of the suspended particles in the Pacific sector of the Southern Ocean. *Mem. Natl Inst. Polar Res.* 50–63 (1983).
31. Martiny, A. C., Vrugt, J. A. & Lomas, M. W. Concentrations and ratios of particulate organic carbon, nitrogen, and phosphorus in the global ocean. *Sci. Data* **1**, 140048 (2014).
32. Garcia, C. A. et al. Nutrient supply controls particulate elemental concentrations and ratios in the low latitude eastern Indian Ocean. *Nat. Commun.* **9**, 4868 (2018).
33. Tanioka, T. et al. Global patterns and predictors of C:N:P in marine ecosystems. *Commun. Earth Environ.* **3**, 1–9 (2022).
34. Fay, A. R. & McKinley, G. A. Global open-ocean biomes: mean and temporal variability. *Earth Syst. Sci. Data* **6**, 273–284 (2014).
35. Moore, C. M. et al. Processes and patterns of oceanic nutrient limitation. *Nat. Geosci.* **6**, 701–710 (2013).
36. Van Mooy, B. A. S. et al. Phytoplankton in the ocean use non-phosphorus lipids in response to phosphorus scarcity. *Nature* **458**, 69–72 (2009).
37. Ustick, L. J., Larkin, A. A. & Martiny, A. C. Global scale phylogeography of functional traits and microdiversity in *Prochlorococcus*. *ISME J.* **17**, 1671–1679 (2023).
38. Kwiatkowski, L., Aumont, O., Bopp, L. & Ciais, P. The impact of variable phytoplankton stoichiometry on projections of primary production, food quality, and carbon uptake in the global ocean. *Glob. Biogeochem. Cycles* **32**, 516–528 (2018).

39. Gerace, S. D., Yu, J., Moore, J. K. & Martiny, A. C. Observed declines in upper ocean phosphate-to-nitrate availability. *Proc. Natl Acad. Sci. USA* **122**, e2411835122 (2025).
40. Kwon, E. Y. et al. Nutrient uptake plasticity in phytoplankton sustains future ocean net primary production. *Sci. Adv.* **8**, eadd2475 (2022).
41. Bindoff, N. L., Cheung, W. W. L. & Kairo, J. G. Changing Oean, Marine Ecosystems, and Dependent Communities. In *Special Report on the Ocean and Cryosphere in a Changing Climate Summary for Policymakers* 447–588 (IPCC, 2019).
42. Platt, T. & Irwin, B. Caloric content of phytoplankton. *Limnol. Oceanogr.* **18**, 306–310 (1973).
43. Smith, A. E. & Morris, I. Pathways of carbon assimilation in phytoplankton from the Antarctic Ocean. *Limnol. Oceanogr.* **25**, 865–872 (1980).
44. Li, W. & Platt, T. Distribution of carbon among photosynthetic end-products in phytoplankton of the eastern Canadian arctic. *J. Phycol.* **18**, 466–471 (1982).
45. Irwin, B., Harrison, W. G., Gallegos, C. L. & Platt, T. Phytoplankton productivity experiments and nutrient measurements in the Labrador Sea, Davis Strait, Baffin Bay and Lancaster Sound from 26 August to 14 September 1978. *Can. Data Rep. Fish. Aquat. Sci.* **213**, 103 (1980).
46. Irwin, B., Dickie, P., Lindley, P. & Platt, T. Phytoplankton productivity in Lancaster sound and approaches during the summer of 1979. *Can. Data Rep. Fish. Aquat. Sci.* **423**, 103 (1984).
47. Irwin, B., Harris, L., Dickie, P., Lindley, P. & Platt, T. Phytoplankton productivity in the Eastern Canadian Arctic during July and August 1980. *Can. Data Rep. Fish. Aquat. Sci.* **386**, 157 (1983).
48. Irwin, B., Harris, L., Hodgson, M., Horne, E. & Platt, T. Primary productivity and nutrient measurements in northern foxe basin, N.W.T. from 27 august to 7 september 1981. *Can. Data Rep. Fish. Aquat. Sci.* **385**, 40 (1983).
49. Smith, R., Gosselin, M., Kattner, G., Legendre, L. & Pesant, S. Biosynthesis of macromolecular and lipid classes by phytoplankton in the Northeast Water Polynya. *Mar. Ecol. Prog. Ser.* **147**, 231–242 (1997).
50. Lee, S. H., Kim, H.-J. & Whitledge, T. E. High incorporation of carbon into proteins by the phytoplankton of the Bering Strait and Chukchi Sea. *Cont. Shelf Res.* **29**, 1689–1696 (2009).
51. Kim, B. K. et al. High lipid composition of particulate organic matter in the northern Chukchi Sea, 2011. *Deep Sea Res. Pt. II* **120**, 72–81 (2015).
52. Choe, K. et al. Spatial patterns of macromolecular composition of phytoplankton in the Arctic Ocean. *Water* **13**, 2495 (2021).
53. Kim, B. et al. Characteristics of the biochemical composition and bioavailability of phytoplankton-derived particulate organic matter in the Chukchi Sea, Arctic. *Water* **12**, 2355 (2020).
54. Fabiano, M., Povero, P. & Danovaro, R. Distribution and composition of particulate organic matter in the Ross Sea (Antarctica). *Polar Biol.* **13**, 525–533 (1993).
55. Fabiano, M., Povero, P. & Danovaro, R. Particulate organic matter composition in Terra Nova Bay (Ross Sea, Antarctica) during summer 1990. *Antarct. Sci.* **8**, 7–13 (1996).
56. Fabiano, M. & Pusceddu, A. Total and hydrolizable particulate organic matter (carbohydrates, proteins and lipids) at a coastal station in Terra Nova Bay (Ross Sea, Antarctica). *Polar Biol.* **19**, 125–132 (1998).
57. Pusceddu, A., Cattaneo-Vietti, R., Albertelli, G. & Fabiano, M. Origin, biochemical composition and vertical flux of particulate organic matter under the pack ice in Terra Nova Bay (Ross Sea, Antarctica) during late summer 1995. *Polar Biol.* **22**, 124–132 (1999).
58. Kim, B. K. et al. Macromolecular compositions of phytoplankton in the Amundsen Sea, Antarctica. *Deep Sea Res. Pt. II* **123**, 42–49 (2016).
59. Misic, C. et al. Factors driving the bioavailability of particulate organic matter in the Ross Sea (Antarctica) during summer. *Hydrobiologia* **851**, 2657–2679 (2024).
60. Jo, N. et al. Different biochemical compositions of particulate organic matter driven by major phytoplankton communities in the Northwestern Ross Sea. *Front. Microbiol.* **12**, 623600 (2021).
61. Intergovernmental Panel On Climate Change. *The Ocean and Cryosphere in a Changing Climate: Special Report of the Intergovernmental Panel on Climate Change* (Cambridge Univ. Press, 2022); https://doi.org/10.1017/9781009157964.
62. Myers, S. S. et al. Increasing CO_2 threatens human nutrition. *Nature* **510**, 139–142 (2014).
63. Loladze, I. Hidden shift of the ionome of plants exposed to elevated CO_2 depletes minerals at the base of human nutrition. *eLife* **3**, e02245 (2014).
64. Kiørboe, T. Phytoplankton growth rate and nitrogen content: implications for feeding and fecundity in a herbivorous copepod. *Mar. Ecol. Prog. Ser.* 229–234 (1989).
65. Jones, R., Flynn, K. & Anderson, T. Effect of food quality on carbon and nitrogen growth efficiency in the copepod Acartia tonsa. *Mar. Ecol. Prog. Ser.* **235**, 147–156 (2002).
66. Jones, R. H. & Flynn, K. J. Nutritional status and diet composition affect the value of diatoms as copepod prey. *Science* **307**, 1457–1459 (2005).
67. Malzahn, A. M., Hantzsche, F., Schoo, K. L., Boersma, M. & Aberle, N. Differential effects of nutrient-limited primary production on primary, secondary or tertiary consumers. *Oecologia* **162**, 35–48 (2010).
68. Lee, R. F., Hagen, W. & Kattner, G. Lipid storage in marine zooplankton. *Mar. Ecol. Prog. Ser.* **307**, 273–306 (2006).
69. Leu, E., Søreide, J. E., Hessen, D. O., Falk-Petersen, S. & Berge, J. Consequences of changing sea-ice cover for primary and secondary producers in the European Arctic shelf seas: Timing, quantity, and quality. *Prog. Oceanogr.* **90**, 18–32 (2011).
70. Søreide, J. E., Leu, E., Berge, J., Graeve, M. & Falk-Petersen, S. Timing of blooms, algal food quality and *Calanus glacialis* reproduction and growth in a changing Arctic. *Glob. Chang. Biol.* **16**, 3154–3163 (2010).
71. Robison, B. H. Deep pelagic biology. *J. Exp. Mar. Biol. Ecol.* **300**, 253–272 (2004).
72. Ahn, S. H. et al. The biochemical composition of phytoplankton in the Laptev and East Siberian seas during the summer of 2013. *Polar Biol.* **42**, 133–148 (2019).

Methods

Macromolecular and ecological model

We simulated the macromolecular composition using the Cell Flux Model (CFM-phyto[23,25]), which is now part of the Darwin model[73], the ecological and biogeochemical module embedded in the Massachusetts Institute of Technology (MIT) general circulation model[74]. The macromolecular model estimates the growth rate of phytoplankton and the cellular composition based on a cellular mass balance of carbon, nitrogen, phosphorus and iron. Carbon is distributed among photosynthetic and electron transport proteins ($Q_C^{Pro-photo}$), biosynthetic proteins ($Q_C^{Pro-bio}$) and a constant 'structural' pool of proteins ($Q_C^{Pro-other}$), which includes nutrient acquisition-related proteins and structural proteins. Although some studies suggests that the relative contribution of nutrient acquisition-related proteins may change, for example, under nutrient limitation[75], we did not explicitly include this effect, as its impact on overall stoichiometry appears limited[15,27]. RNA (Q_C^{RNA}), DNA (Q_C^{DNA}), chlorophyll (Q_C^{Chl}), carbon in phospholipids in the thylakoid membrane (Q_C^{PLip}), carbon storage as carbohydrates and lipids (Q_C^{Stor}), carbon associated with nitrogen storage (Q_N^{NStor}) and constant pool of structural carbohydrates and lipids (Q_C^{Other}). Q_C^i are the mol C in macromolecules per mol C; see Supplementary Table 7 for symbol definition and units:

$$Q_C = Q_C^{Pro-photo} + Q_C^{Pro-bio} + Q_C^{Pro-other} + Q_C^{RNA} + Q_C^{DNA} + Q_C^{Chl} + Q_C^{PLip} + \\ + Q_C^{Stor} + Q_N^{NStor} Y_{Nsto}^{C:N} + Q_C^{Other}. \quad (1)$$

Nitrogen in the cell is distributed among proteins ($Q_C^{Pro}/Y_{Pro}^{C:N}$), where $Y_{Pro}^{C:N}$ is the molar carbon-to-nitrogen ratio in proteins, RNA (Q_N^{RNA}), DNA (Q_N^{DNA}), chlorophyll (Q_N^{Chl}) and nitrogen storage (Q_N^{NStor}). Q_N^i are in mol N in macromolecules per mol C:

$$Q_N = Q_C^{Pro}/Y_{Pro}^{C:N} + Q_N^{RNA} + Q_N^{DNA} + Q_N^{Chl} + Q_N^{NStor}. \quad (2)$$

Cellular phosphorus is distributed between RNA (Q_P^{RNA}), DNA ($Q_C^{DNA} Y_{DNA}^{P:C}$), where $Y_{DNA}^{P:C}$ is the molar phosphorous-to-carbon ratio in DNA, Q_P^{Thy} is phosphorous in the thylakoid membrane, Q_P^{Stor} is phosphorus storage and Q_P^{Other} is the small constant phosphorous pool. Q_P^i are in mol P in macromolecules per mol C:

$$Q_P = Q_P^{RNA} + Q_C^{DNA} Y_{DNA}^{P:C} + Q_P^{Thy} + Q_P^{Stor} + Q_P^{Other}. \quad (3)$$

Iron in the cell is associated with photosynthesis proteins (Q_{Fe}^{Pho}) and iron storage (Q_{Fe}^{Stor}). Q_{Fe}^i are in mol Fe in macromolecules per mol C:

$$Q_{Fe} = Q_{Fe}^{Pho} + Q_{Fe}^{Stor}. \quad (4)$$

The molar fractions of these macromolecules are a function of light, temperature and nutrient uptake. Chlorophyll, Q_C^{Chl}, has a negative relationship with light and a positive relationship with growth rate:

$$Q_C^{Chl} = \frac{(1+E)}{P(I)}\mu + \frac{m}{P(I)}, \quad (5)$$

where E is respiratory costs associated with cell synthesis (unitless), m is maintenance respiration rate (per day), μ is growth rate (per day) and $P(I)$ is photosynthesis rate (mol C (mol C in Chl)$^{-1}$ day^{-1}), which is a function of light (I; μmol m^{-2} s^{-1}):

$$P(I) = V_I^{max}\left(1 - \exp^{-A_I I}\right), \quad (6)$$

where V_I^{max} is the maximum chlorophyll-specific photosynthetic rate (mol C (mol C in Chl)$^{-1}$ day^{-1}) and A_I is the absorption cross-section and turnover time of the photosynthesis unit (m^2 s μmol^{-1}). Photosynthetic proteins ($Q_C^{Pro-photo}$) and phosphorous in the thylakoid membrane (Q_P^{Thy}) positively relate to chlorophyll:

$$Q_C^{Pro-photo} = A_{Pho} Q_C^{Chl} \quad (7)$$

$$Q_P^{Thy} = A_{Pho}^{P:Chl} Q_C^{Chl} \quad (8)$$

$$Q_{Fe}^{Pho} = A_{Pho}^{Fe:Chl} Q_C^{Chl}. \quad (9)$$

Here, A_{Pho} (mol C (mol C in Chl)$^{-1}$), $A_{Pho}^{P:Chl}$ (mol P (mol C in Chl)$^{-1}$) and $A_{Pho}^{Fe:Chl}$ (mol Fe (mol C in Chl)$^{-1}$) are stoichiometric parameters (Supplementary Table 9). Biosynthetic protein and RNA content are assumed to scale linearly with temperature-normalized growth rate:

$$Q_C^{Pro-bio} = \frac{A_{bio}}{Arr}\mu \quad (10)$$

$$Q_P^{RNA} = \frac{A_P^{RNA}}{Arr} Q_C^{Pro}\mu + Q_{P,min}^{RNA}. \quad (11)$$

Here, $Q_C^{Pro-bio}$ is carbon allocation to biosynthetic proteins (mol C (mol C)$^{-1}$), and Q_P^{RNA} is the phosphorous allocated to RNA (mol P (mol C)$^{-1}$). A_{bio} (mol C (mol C)$^{-1}$ day) and A_P^{RNA} (mol P (mol C)$^{-1}$ day) are proportionality constants for biosynthetic protein and RNA investments as a function of growth rate. $Q_{P,min}^{RNA}$ is the minimum RNA quota at growth rate (mol P (mol C)$^{-1}$), and Arr is the temperature dependencies on metabolism[24], based on the Arrhenius equation

$$Arr = \exp\left(-\frac{E_a}{R} \times \left(\frac{1}{T} - \frac{1}{T_{ref}}\right)\right), \quad (12)$$

where E_a is the activation energy (equal to 70,000 J mol^{-1})[24], R is the universal gas constant and T_{ref} is the reference temperature (293 K).

These cellular balances for each element, without the storage component, yield trinomial equation for growth rate, which solve numerically. The minimum growth rate based on the cellular mass balance is selected to be the growth rate based on the Liebig's minimum law. After detecting the limit element from the cellular mass balances, the storage macromolecules of the non-limited elements are calculated, and the nutrient uptake of these elements are reduced[25].

These macromolecule pools are resolved for two phytoplankton types: small phytoplankton (0.41 μm^3) broadly representing picocyanobacteria (for example, *Prochlorococcus*), and large phytoplankton (46 μm^3) representing larger eukaryotes (for example, diatoms). Both phytoplankton are independently grazed by a single grazer. The two phytoplankton types differ in their maximum photosynthesis rates, maximum nutrient uptake rates, nutrient-half saturation constant, sinking rates and palatability to grazers (Supplementary Table 8). We assume a Holling type 2 grazing functional response modified by prey preference, prey availability and temperature. We assume that grazers regulate their elemental composition by keeping internal quotas within a specific range (Supplementary Table 9). When the stoichiometry of phytoplankton and zooplankton is mismatched, excess elements are routed to dissolved organic matter and POM. In this way, zooplankton decouples the stoichiometry of phytoplankton from that of POM and dissolved organic matter[76]. Dead phytoplankton and zooplankton are also routed into the particulate and dissolved pools. All these tracers are advected and mixed by the physical fields (see the following section). The mortality and remineralization of POM and dissolved organic matter follow the same temperature dependence, with an activation energy of 34,000 J mol^{-1} (ref. 76).

Physical model

The biogeochemical tracers are transported and mixed by the oceanic component of the MIT Integrated Global System Model (IGSM)[77–79]. The IGSM is an Earth system model of intermediate complexity, with a zonally averaged two-dimensional atmosphere and three-dimensional (3D) ocean circulation model, and is coupled to terrestrial, atmospheric, economic and dynamic sea-ice models. The atmospheric model includes several greenhouse gases (CO_2, CH_4 and N_2O) and several aerosols (SO_2 and black carbon). The 3D ocean model is forced with wind stress (detrended wind speed from the National Center for Environmental Prediction (NCEP) reanalysis[80]). For each year of the simulation, we randomly sample from the computed wind stress (1948–2007). This approach produces a realistic El Niño–Southern Oscillation signal, although not corresponding to the exact historical years. For simplicity, the wind stress forcing is not impacted by climate change, because there are considerable model uncertainties. The terrestrial component addresses surface heat fluxes, hydrological processes, and carbon and nitrogen dynamics, and the economic component is a human activity model that predicts gas emissions through population and economic growth estimations. We refer the reader to the citation above for more information on the different components of the model.

The 3D oceanic component of the IGSM is the MIT General Circulation Model, configured here with a longitudinal resolution of 2.5°, latitudinal resolution of 2° and 22 vertical depth levels: 10 m at the surface, increasing to 500 m at the bottom. To integrate the biogeochemical tracers, we use physical fields from previous forward runs where a specific set of parameters, coupling procedures and flux adjustment schemes were applied as in ref. 77. The monthly mean fields that drive the biogeochemical simulations include 3D velocities, mixing parameters, potential salinity, temperature, freshwater flux and sea-ice cover.

Our model calculates the absorption and scattering of spectral light (average 25-nm bands from 400 to 700 nm) through the water column, which is a function of chlorophyll, phytoplankton carbon, particulate detritus (POM) and water molecules[81]. Input light fields are monthly averages of direct and diffusive light in each waveband, estimated from the Ocean–Atmosphere Spectral Irradiance Model (OASIM), which accounts for role of clouds, aerosols and water vapours in the atmosphere as well as surface roughness and reflectance at the ocean–atmosphere interface[82]. Surface forcings of PAR and iron dust flux are derived from SeaWiFS and an atmospheric transport and chemical model[83], respectively. Light and dust fields are climatological monthly means and did not change in the future projection described below.

Simulation set-up

Phase 1: Pre-industrial equilibrium conditions. In this experiment, the macromolecular and ecosystem model is initialized with observed distributions of phosphate, nitrate, iron, oxygen, alkalinity and carbon tracers, and integrated for 50 years with atmospheric carbon dioxide fixed at the pre-industrial mixing ratio of 278 ppmv. After this spin-up, the biogeochemical tracers reach a quasi-steady state and are in reasonable agreement with global observations (Supplementary Fig. 6).

Phase 2: Pre-industrial control. The pre-industrial conditions were used for another 240 years. This experiment provides a measure of the biogeochemical and ecological drifts (Supplementary Fig. 7).

Phase 3: 1860–1990 transient response. In this experiment, the tracers are initialized from the equilibrium state of phase 1. Here, the climate system is forced with observed solar irradiance, greenhouse gases, aerosols and tropospheric ozone. Natural emissions of methane and nitrogen, as well as terrestrial carbon uptake by land, are provided by the coupled IGSM models.

Phase 4: 1991–2100 transient response. In this experiment, the tracers are initialized from the 1990 tracer concentrations of phase 3 and are transported and mixed by the fully coupled model. In addition, the economic model provides emissions of greenhouse gases and aerosols, and the climate model simulates the atmospheric chemistry and the land and ocean biogeochemical cycles. We use a high-emissions scenario consistent with the SSP5-8.5 scenario and a model configuration with a climate sensitivity of 3.0 °C.

Uniqueness and limitations of the model

Our method is built upon basic knowledge from extensive laboratory experimental work samples[7,15,84]. Nevertheless, some gaps in our knowledge still exist that may introduce uncertainty in our results. A key limitation of the model is the allocation of carbon and energy stores between lipid and carbohydrate. Here, we simply assume equal allocation of storage carbon between lipid and carbohydrates. While this is clearly an oversimplification, there is some empirical support from field observations[27], and no obvious mechanistic representation currently exists to our knowledge. We suggest that new laboratory experiments linked to this modelling goal would be valuable, for example, to examine and quantify trade-offs between the energetic and enzymatic costs of synthesis and their relative value as energy stores.

Our modelled ecosystem includes two phytoplankton (large and small) and one zooplankton. We recognize that the simplified representation of ecosystem structure has limitations (for example refs. 85,86). Here, we choose this limited system to focus on the physiological dynamics of macromolecular allocation in climate-scale simulations. We note that, even with this idealized ecosystem, our model successfully captures large-scale patterns of macromolecular and elemental composition across the ocean (Extended Data Figs. 2 and 3). The interaction with a highly taxonomically and trophically resolved system is an interesting avenue for future research.

Calculation of global averages of ratios and drift correction

The depth-integrated ratios of Protein–C:C and Carb+Lipid–C:C in maps (Fig. 1a,b) were calculated by setting

$$X:C=\frac{\sum_i\left(\left(X_i^1c_i^1+X_i^2c_i^2\right)\mathrm{Vol}_i\right)}{\sum_i\left(\left(c_i^1+c_i^2\right)\mathrm{Vol}_i\right)}, \tag{13}$$

where X_i^1 and X_i^2 are cellular carbon allocation to proteins and to carbohydrates + lipids (mol C (mol C)$^{-1}$) of phytoplankton 1 and 2 integrated over depth i (m), c_i^1 and c_i^2 are the carbon concentration of the two phytoplankton (mmol C m^{-3}), and Vol_i is the grid volume (m^3).

Simulated, drift-corrected absolute changes between the depth-integrated means in Figs. 2–4 were calculated by setting

$$\Delta\mathrm{clim}=\overline{X:C}^{\mathrm{clim}}_{2070:2100}-\overline{X:C}^{\mathrm{ctrl}}_{2070:2100}. \tag{14}$$

Here, $\overline{X:C}^{\mathrm{clim}}_{2070:2100}$ is the projected means (phase 4), and $\overline{X:C}^{\mathrm{ctrl}}_{2070:2100}$ is 'drifting' pre-industrial conditions (phase 2) from 2070 to 2100, both calculated from equation (13).

Global, volume- and mass-weighted means were calculated as

$$X:C'=\frac{\sum_l\sum_l\sum_l\left(\left(X_{i,j,l}^1c_{i,j,l}^1+X_{i,j,l}^2c_{i,j,l}^2\right)\mathrm{Vol}_{i,j,l}\right)}{\sum_l\sum_l\sum_l\left(\left(c_{i,j,l}^1+c_{i,j,l}^2\right)\mathrm{Vol}_{i,j,l}\right)}. \tag{15}$$

Here i, j and l are depth, latitude and longitude, respectively.

Simulated, drift-corrected percentage changes in the global means shown in Extended Data Figs. 5a–c and 6c–e were calculated as

$$\Delta\mathrm{clim}\ (\%)=\frac{X'^{\mathrm{clim}}_{1870:2100}-X'^{\mathrm{ctrl}}_{1870:2100}}{X'^{\mathrm{ctrl}}_{1870}}\times 100, \tag{16}$$

where $X'^{\mathrm{clim}}_{1870:2100}$ is the time evolution of global means from 1870 to 2100 in the climate simulations (phases 3 and 4), and $X'^{\mathrm{ctrl}}_{1870:2100}$ is the corresponding time evolution in the 'drifting' control (simulation phase 2). $X'^{\mathrm{ctrl}}_{1870}$ is the initial value of the control simulation in 1870, which is equal to $X'^{\mathrm{clim}}_{1870}$.

Data availability

All data are available in the Article or its Supplementary Information. The model outputs used in this study, the Excel file containing the macromolecular dataset (Supplementary Table 1) and the MATLAB scripts used to generate the figures are available via Zenodo at https://doi.org/10.5281/zenodo.15070334 (ref. 87).

Code availability

To run the model, download the code and input archives available via Zenodo at https://doi.org/10.5281/zenodo.15070334 (ref. 87). The Darwin model package source code, including the macromolecular composition developments implemented by the coauthors, is available via GitHub at https://github.com/darwinproject/darwin3/releases/tag/darwin_ckpt69j (ref. 88). The original model description is given in ref. 73.

References

73. Follows, M. J., Dutkiewicz, S., Grant, S. & Chisholm, S. W. Emergent biogeography of microbial communities in a model ocean. *Science* **315**, 1843–1846 (2007).
74. Marshall, J., Adcroft, A., Hill, C., Perelman, L. & Heisey, C. A finite-volume, incompressible Navier Stokes model for studies of the ocean on parallel computers. *J. Geophys. Res. Oceans* **102**, 5753–5766 (1997).
75. Garcia, N. S. et al. Proteome trait regulation of marine *Synechococcus* elemental stoichiometry under global change. *ISME J.* **18**, wrae046 (2024).
76. Follows, M., Dutkiewicz, S. & Oliver, J. Darwin Package (DARWIN, 2022); https://darwin3.readthedocs.io/en/latest/phys_pkgs/darwin.html
77. Monier, E. et al. Toward a consistent modeling framework to assess multi-sectoral climate impacts. *Nat. Commun.* **9**, 660 (2018).
78. Sokolov, A. et al. Description and evaluation of the MIT Earth System Model (MESM). *J. Adv. Model. Earth Syst.* **10**, 1759–1789 (2018).
79. Dutkiewicz, S., Sokolov, A., Scott, J. & Stone, P. *A Three-Dimensional Ocean–Seaice–Carbon Cycle Model and its Coupling to a Two-Dimensional Atmospheric Model: Uses in Climate Change Studies* (MIT Joint Program on the Science and Policy of Global Change, 2005).
80. Kalnay, E. et al. The NCEP/NCAR 40-year reanalysis project. *Bull. Am. Meteorol. Soc.* **77**, 437–470 (1996).
81. Dutkiewicz, S. et al. Capturing optically important constituents and properties in a marine biogeochemical and ecosystem model. *Biogeosciences* **12**, 4447–4481 (2015).
82. Gregg, W. W. & Casey, N. W. Skill assessment of a spectral ocean–atmosphere radiative model. *J. Mar. Syst.* **76**, 49–63 (2009).
83. Luo, C. et al. Combustion iron distribution and deposition. *Glob. Biogeochem. Cycles* **22**, 2007GB002964 (2008).
84. Healey, F. P. Interacting effects of light and nutrient limitation on the growth rate of *Synechococcus linearis* (Cyanophyceae). *J. Phycol.* **21**, 134–146 (1985).
85. Rohr, T., Richardson, A. J., Lenton, A., Chamberlain, M. A. & Shadwick, E. H. Zooplankton grazing is the largest source of uncertainty for marine carbon cycling in CMIP6 models. *Commun. Earth Environ.* **4**, 212 (2023).
86. Follett, C. L. et al. Trophic interactions with heterotrophic bacteria limit the range of *Prochlorococcus*. *Proc. Natl Acad. Sci. USA* **119**, e2110993118 (2022).
87. Sharoni, S. Supplementary material for: Biochemical remodeling of phytoplankton cell composition under climate change. *Zenodo* https://doi.org/10.5281/zenodo.15070334 (2026).
88. Campin, J.-M. et al. MIT General Circulation Model master code and documentation. *Zenodo* https://doi.org/10.5281/zenodo.1409237 (2026).

Acknowledgements

S.S. thanks all the members in the group of M. Follows and M. Frada for fruitful discussion and comments. We thank the Interuniversity Institute for Marine Sciences in Eilat for hosting S.S. We thank the scientists at the Bedford Institute of Oceanography (Fisheries and Oceans Canada) for their efforts in collecting and curating this valuable dataset and making it available to future researchers. S.S. acknowledges support from the Simons Foundation (grant LS-FMME-00004212), Y. Hanadiv (Rothschild Foundation) and the Fulbright Israel postdoctoral fellowships. K.I. acknowledges support from the Simons Foundation (grants 544338 and LS-ECIAMEE-00001549). M.J.F. and S.D. acknowledge support from the Simons Foundation CBIOMES (grant 549931). S.D. also acknowledges support from the public and private funders of the MIT Center for Sustainability Science and Strategy.

Author contributions

S.S., K.I. and M.J.F. conceived the study. The methodology was developed by S.S., S.D., O.J., K.I., E.M. and M.J.F. The formal analysis and investigation were performed by S.S. Visualization was carried out by S.S. Data curation was performed by S.S., K.I., O.J., Z.V.F., A.I. and M.M.A. Funding was acquired by S.S., K.I. and M.J.F. Supervision was provided by M.J.F. The original draft of the manuscript was written by S.S. and K.I., and all authors, including M.J.F., S.D., Z.V.F., A.I. and E.M., contributed to review and editing

Competing interests

The authors declare no competing interests.

Additional information

Extended data is available for this paper at https://doi.org/10.1038/s41558-026-02598-w.

Supplementary information The online version contains supplementary material available at https://doi.org/10.1038/s41558-026-02598-w.

Correspondence and requests for materials should be addressed to Shlomit Sharoni or Keisuke Inomura.

Peer review information *Nature Climate Change* thanks Sang Lee and the other, anonymous, reviewer(s) for their contribution to the peer review of this work.

https://doi.org/10.1038/s41558-026-02598-w

Extended Data Table 1 | Mass-weighted global means of modeled macromolecular composition (% mol C in macromolecule/mol C)

Macromolecule	Molar Percentage (%)
Proteins	48.1
Carbohydrates	21.7
Lipids	23.3
RNA	0.4
DNA	0.1
Chlorophyll-a	1.4
N-Storage (Cyanophycin)	5.0

https://doi.org/10.1038/s41558-026-02598-w

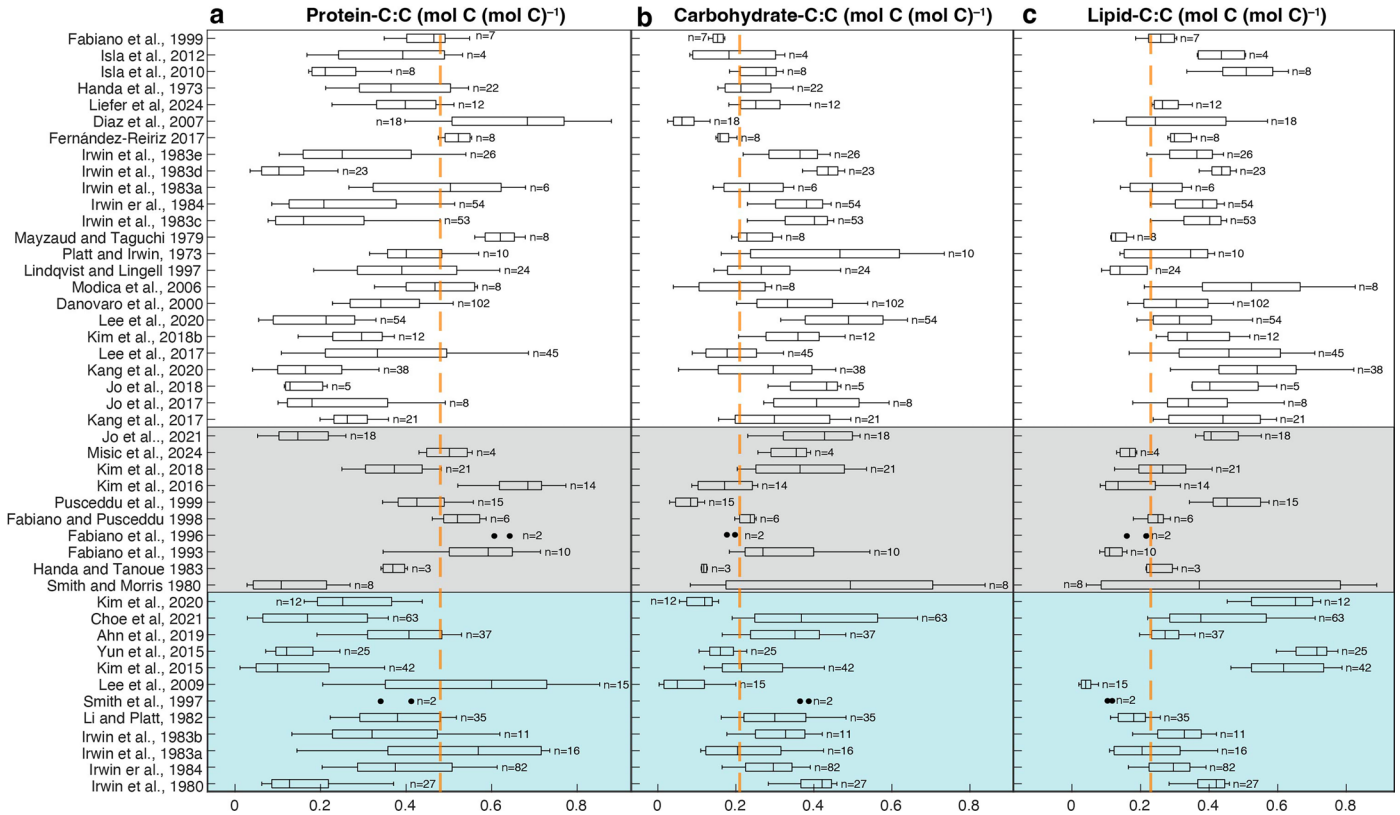

Extended Data Fig. 1 | Macromolecular field data compilation. (**a**) Protein–C:C, (**b**) carbohydrate–C:C, and (**c**) lipid–C:C are summarized for each study (mol C (mol C)$^{-1}$). Box plots show the median (50th percentile) as the center line of the interquartile range (25th–75th percentiles) as the box bounds. Whiskers represent the 5th and 95th percentiles of the data. Numbers in parentheses are the number of observations by study. For ratios with fewer than three observations, values are displayed as individual points. The vertical orange line indicates the model's estimated global mean values. Blue and gray shaded areas indicate the Arctic and Antarctic samples, respectively.

https://doi.org/10.1038/s41558-026-02598-w

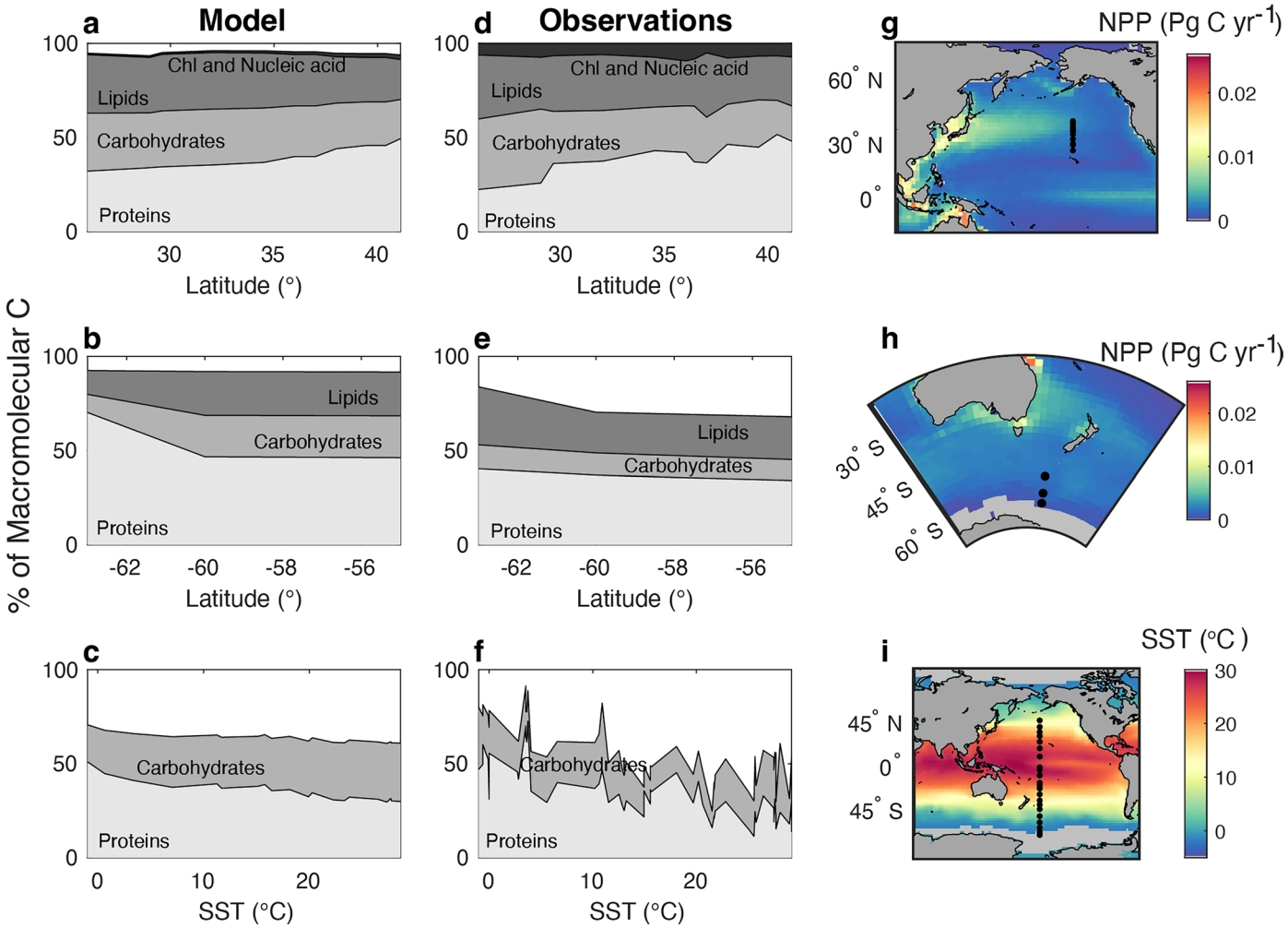

Extended Data Fig. 2 | Comparison between modeled and observed macromolecular carbon allocation across latitudinal and temperature gradients in the Pacific and Southern Oceans. Model results (**a**–**c**) of cellular allocation (mol C (mol C)$^{-1}$) to proteins, carbohydrates, lipids, and chlorophyll and nucleic acids across latitude (top and middle columns) and sea surface temperature (SST) (bottom column). In the second row, observational data from (**d**) Liefer et al., 2024[27] (**e**) Handa & Tanoue, 1983[30] and (**f**) Handa et al., 1973[29], showing macromolecular allocation trends at corresponding latitudinal transects and SST gradients. (**g**–**i**) Maps displaying the geographic locations of observational sampling sites. Heat maps in the upper and middle rows show the depth-integrated decade mean of net primary productivity (Pg C/yr), and the bottom map shows sea-surface temperature (°C). See Supplementary Methods for model-data comparison procedure.

https://doi.org/10.1038/s41558-026-02598-w

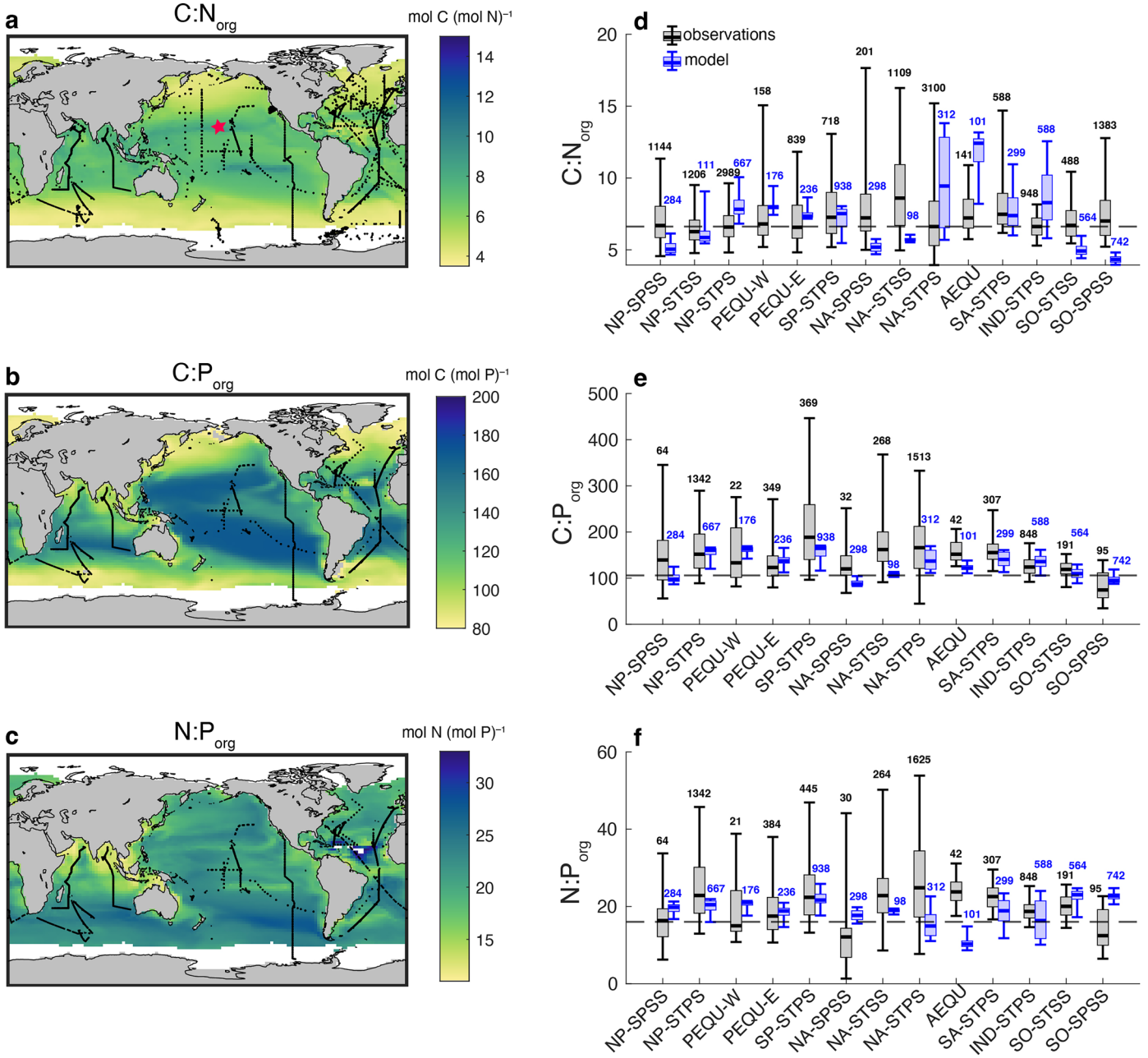

Extended Data Fig. 3 | Comparison between modeled and observed organic matter C:N, C:P, and N:P. Depth-integrated (0–170 m) annual averages under pre-industrial equilibrium conditions are shown for modeled (**a**) $C:N_{org}$ (mol C (mol N)$^{-1}$), (**b**) $C:P_{org}$ (mol C (mol P)$^{-1}$), and (**c**) $N:P_{org}$ (mol N (mol P)$^{-1}$), encompassing phytoplankton and particulate organic matter. Points mark sampling locations. Panels (**d**–**f**) show comparisons between modeled and observed $C:N_{org}$, $C:P_{org}$, and $N:P_{org}$ (molar ratios), at different ecoprovinces defined in Fig. S1[34]. Gray boxplots summarize the observed distributions[31–33], with the box representing the interquartile range (25th–75th percentiles) and the center indicating the median (50th percentile). Whiskers extend to the 5th and 95th percentiles. Each observation represents an independent sampling location. The number of observations contributing to each ecoprovince is reported in black. Blue boxplots summarize the modeled values across grid cells, with the number of grid cells in each ecoprovince is reported in blue. The dashed-black line indicates the Redfield ratio ($C:N_{org}$ = 6.625, $C:P_{org}$ = 106, $N:P_{org}$ = 16). The acronyms for ecoprovinces are explained in Fig. S1.

https://doi.org/10.1038/s41558-026-02598-w

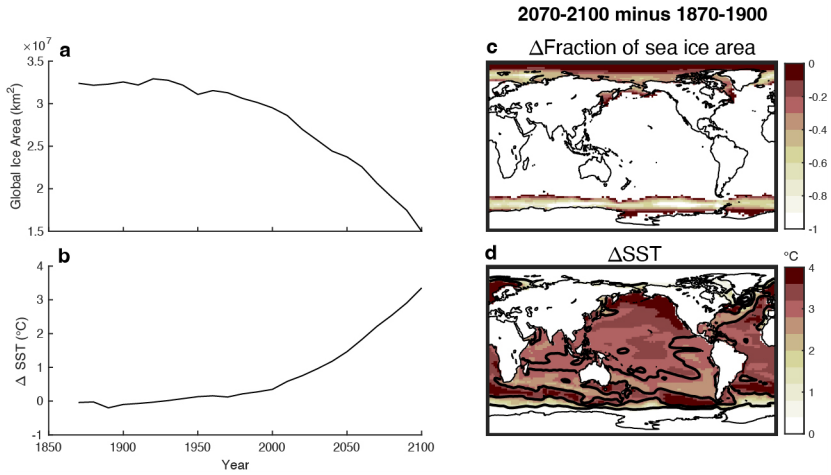

Extended Data Fig. 4 | Projected temperature and sea ice changes. Drift-corrected global mean of **(a)** extent of ocean covered by sea ice (km^2) and (**b**) global mean sea surface temperature (SST; °C). Right panels show spatial patterns of simulated change (2080–2100 relative to 1870–1900) in (**c**) fraction of sea ice area (unitless), and (**d**) SST.

https://doi.org/10.1038/s41558-026-02598-w

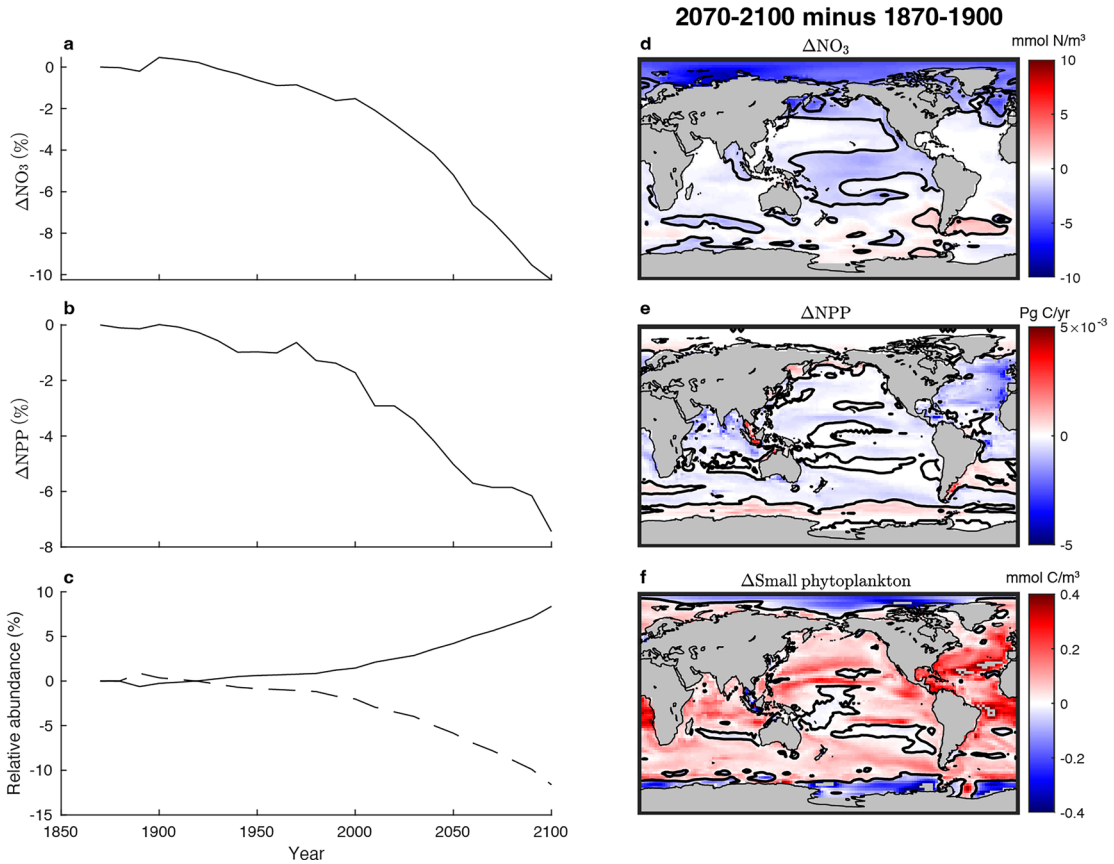

Extended Data Fig. 5 | Surface nitrate concentration, net primary productivity, and relative abundance of small phytoplankton over the 21st century. Simulated percentages of global changes of (**a**) upper 100 m nitrate concentrations (mmol/m^3), (**b**) upper 100 m net primary productivity (Pg C/yr), and (**c**) relative concentration of small (solid) and large (dashed) phytoplankton integrated over the top 170 m. Panels **d**–**f** show spatial patterns of simulated absolute change in these variables averaged over 2080–2100 relative to 1870–1900 for high emission scenario. All the values are calculated as the difference between the climate-change simulations and the baseline control simulation (see Methods).

https://doi.org/10.1038/s41558-026-02598-w

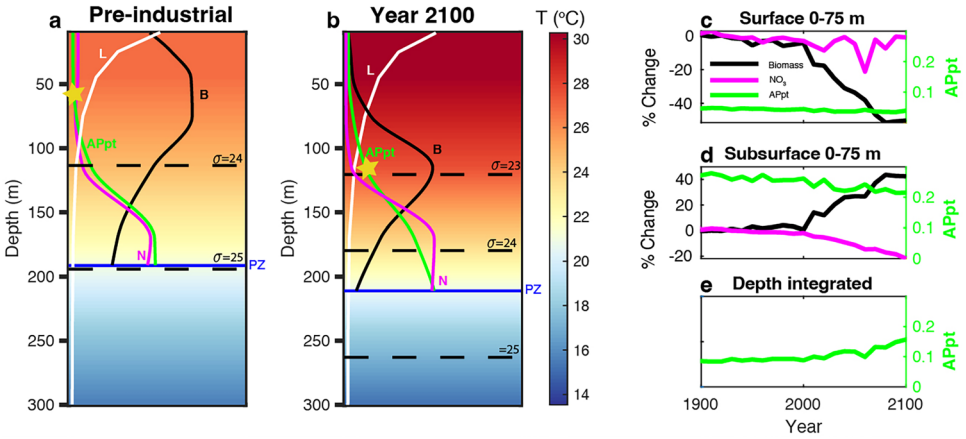

Extended Data Fig. 6 | Vertical profiles of temperature, cellular allocation to photosynthetic proteins, biomass, and nutrients in the subtropical Pacific (the location marked with a red star in Extended Data Fig. 3a). (**a**, **b**) Vertical profiles of photosynthetically active radiation (L, white), total phytoplankton biomass (B, black), cellular investment in photosynthetic proteins (APpt, green), and bioavailable nitrogen concentrations (N, magenta). All values are normalized to their maximum value. Panel **a** shows the vertical profiles of pre-industrial conditions, and Panel **b** shows simulated change at the end of the 21st century under a high-emission climate change scenario. The background colormap represents temperature (°C). The gold stars mark the cellular investments in photosynthetic proteins at depth where biomass is at its maximum. Dashed black horizontal lines denote isopycnal surfaces at σ = 23, 24, and 25 kg/m^3. The blue horizontal line indicates the depth of the photic zone (PZ), where the photosynthetically active radiation is reduced to 1% of its surface value. (**c**–**e**) Drift-corrected percentage of changes of phytoplankton biomass (black, left y-axis; %), nitrate concentration (magenta, left y-axis; %), and cellular allocation to photosynthetic proteins (green, right y-axis; mol C in proteins/mol C) over the 21st century of (**c**) surface (0–75 m) phytoplankton, (**d**) subsurface (75–170 m) phytoplankton and (e) depth-integrated values (0–170 m).

https://doi.org/10.1038/s41558-026-02598-w

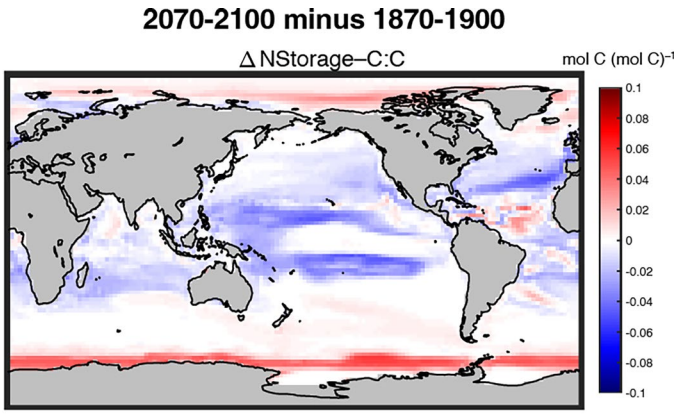

Extended Data Fig. 7 | Projected change in cellular allocation to nitrogen storage. Drift-corrected simulated change (2070–2100 relative to 1870–1900) of depth-integrated cellular allocation to nitrogen storage (mol C (mol C)$^{-1}$).

https://doi.org/10.1038/s41558-026-02598-w

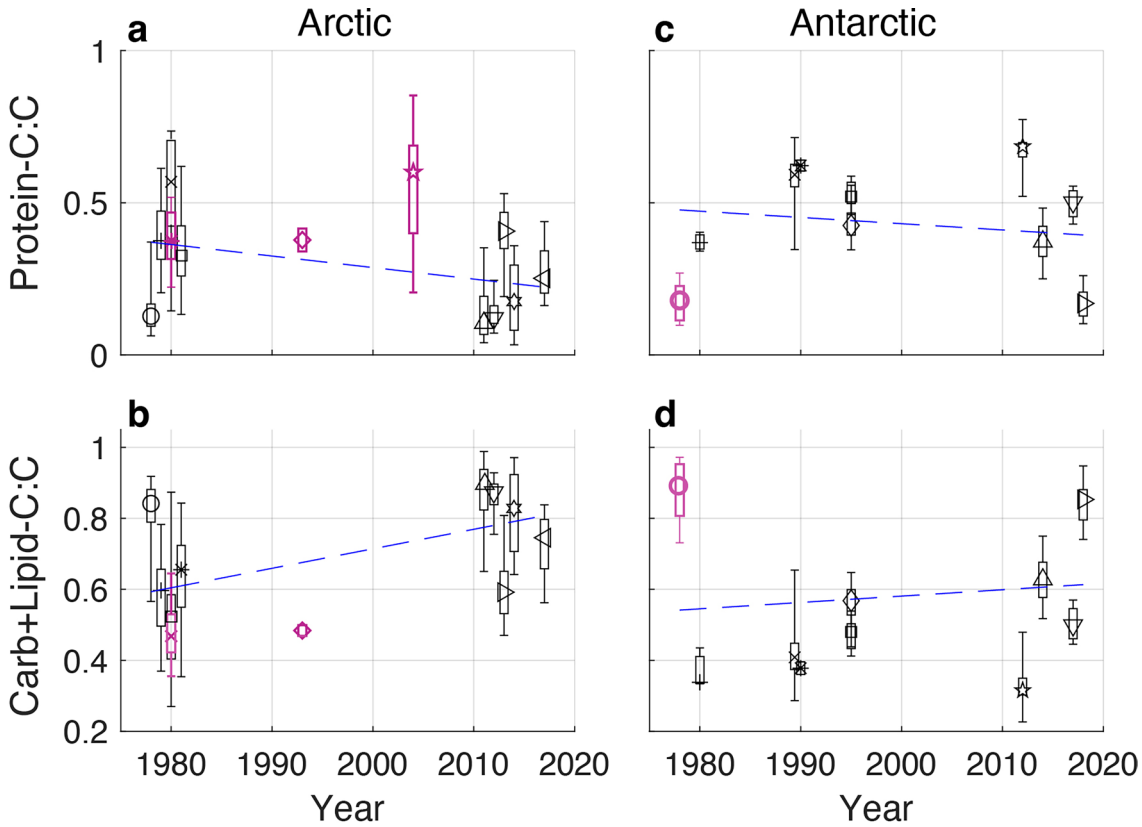

Extended Data Fig. 8 | Temporal trends in macromolecular composition in polar phytoplankton. Arctic **(a)** protein (n_{obs}=359) and **(b)** combined carbohydrate and lipid content (n_{obs}=342). Arctic data were obtained from: Irwin et al., 1980[45] (circle), Irwin et al., 1984[46] (plus), Irwin et al., 1983a[47] (square), Li and Platt, 1982[44] (cross), Smith et al., 1997[49] (star), Lee et al., 2009[50] (diamond), Kim et al., 2015[51] (upward triangle), Yun et al., 2015[11] (downward triangle), Ahn et al., 2019[72] (right triangle), Choe et al., 2021[52] (pentagon), and Kim et al., 2020[53] (left triangle). Antarctic **(c)** protein (n_{obs}=96) and **(d)** combined carbohydrate and lipid content (n_{obs}=101). Antarctic data was obtained from: Smith and Morris, 1980[43] (circle), Handa and Tanoue, 1983[30] (plus), Fabiano et al., 1993[54] (cross), Fabiano et al., 1996[55] (star), Fabiano and Pusceddu 1998[56] (square), Pusceddu et al., 1999[57] (diamond), Kim et al., 2016[58] (pentagon), Kim et al., 2018[10] (upward triangle), Misic et al., 2024[59] (downward triangle), and Jo et al., 2021[60] (right triangle). Box plots show the median (25th percentile) as the center line of the interquartile range (25th–75th percentiles) as the box bounds. Whiskers represent the 5th and 95th percentiles of the data. For linear regression statistics, see Table S6. Pink indicates measurements made with carbon isotope labeling.